coatings

MDPI

Article

Laser Processing of Liquid Feedstock Plasma-Sprayed Lithium Titanium Oxide Solid-State-Battery Electrode

Arman Hasani [1,*], Mathis Luya [2], Nikhil Kamboj [1], Chinmayee Nayak [1], Shrikant Joshi [3], Antti Salminen [1], Sneha Goel [1,4] and Ashish Ganvir [1]

[1] Department of Mechanical and Materials Engineering, Faculty of Technology, University of Turku, 20014 Turku, Finland; nikhil.kamboj@utu.fi (N.K.); chinmayee.nayak@utu.fi (C.N.); antti.salminen@utu.fi (A.S.); sneha.goel@utu.fi (S.G.); ashish.ganvir@utu.fi (A.G.)
[2] Seatech Engineering School, University of Toulon, 13009 Marseille, France; mathis.luya.23@seatech.fr
[3] Department of Engineering Science, University West, 461 32 Trollhättan, Sweden; shrikant.joshi@hv.se
[4] Advanced Materials for Nuclear Energy, VTT Technical Research Centre of Finland, 02150 Espoo, Finland
* Correspondence: arman.hasani@utu.fi

Abstract: The astonishing safety and capacity characteristics of solid-state-batteries are encouraging researchers and companies to work on the manufacturing, development, and characterization of battery materials. In the present work, the effects of laser beam interaction with a liquid feedstock plasma-sprayed ceramic solid-state-battery (SSB) material coating were studied. Lithium Titanium Oxide (LTO) in the form of an aqueous suspension consisting of submicron powder particles was plasma-sprayed for the first time using a high-power axial III plasma torch on an aluminum substrate. The plasma-sprayed LTO coating suspension was subsequently post-processed using a fiber laser. The energy input of the laser beam on the surface of the deposited layer was the main variable. By varying the laser power and laser processing speed, the energy input values were varied, with values of 3.8 J/mm^2, 9.6 J/mm^2, 765.9 J/mm^2, and 1914.6 J/mm^2, and their effects on some key characteristics such as laser-processed zone dimensions and chemical composition were investigated. The results indicated that changing the laser beam parameter values has appreciable effects on the geometry, surface morphology, and elemental distribution of laser-processed zones; for instance, the highest energy inputs were 33% and 152%, respectively, higher than the lowest energy input.

Keywords: ceramic solid-state lithium-ion battery; laser processing; liquid feedstock; lithium titanium oxide (LTO); suspension plasma spray

Citation: Hasani, A.; Luya, M.; Kamboj, N.; Nayak, C.; Joshi, S.; Salminen, A.; Goel, S.; Ganvir, A. Laser Processing of Liquid Feedstock Plasma-Sprayed Lithium Titanium Oxide Solid-State-Battery Electrode. *Coatings* **2024**, *14*, 224. https://doi.org/10.3390/coatings14020224

Academic Editor: Torsten Brezesinski

Received: 4 January 2024
Revised: 7 February 2024
Accepted: 8 February 2024
Published: 12 February 2024

1. Introduction

To convert chemical energy directly into electrical energy by utilizing an electrochemical oxidation–reduction (redox) reaction, the transfer of electrons from one material to another via an electric circuit is needed, and the electric device in which these reactions take place is called a battery. Lithium-ion (Li-ion) batteries are the most common type of batteries which have an unmatchable combination of high energy and power density, high energy efficiency, high safety, environmental friendliness, etc., in comparison to traditional batteries. These remarkable advantages make them one of the most promising energy device candidates for industries spanning across several applications such as electric vehicles, portable electronics, renewable energy storage, aerospace and satellites, medical devices, the Internet of Things, etc. [1–3].

In common Li-ion batteries, along with metallic current collectors, there are three primary constituents which are an anode, a cathode, and a liquid electrolyte. On the other hand, in SSBs (sometimes also referred to as all-solid-state-batteries (ASSBs)), the liquid electrolyte that is in traditional Li-ion batteries is replaced by a "solid-state" electrolyte, serving the purpose of both an electrolyte as well as a separator. SSBs are perfect substitutes for conventional Li-ion batteries due to their higher energy and power density, higher

safety, wide electrochemical stability window as compared to the present organic polymer electrolyte batteries, absence of electrolyte leakage and vaporization of liquid electrolytes, ease of miniaturization, and long cycle life [4–6].

Historically, much effort has been put into developing alternative materials as well as manufacturing technologies for primary ASSB constituents, especially solid electrolytes. Despite some examples of already commercialized state-of-the-art (SOTA) materials for cathodes, anodes, and electrolytes existing, such as $Li_4Ti_5O_{12}$ (LTO), $LiNi_{1/3}Mn_{1/3}Co_{1/3}O_2$ (NMC), and $Li_7La_3Zr_2O_{12}$ (LLZO), respectively, along with already commercialized manufacturing technologies, the adoption of ASSBs by various industries is still scarce [7–9]. The main issues remaining to be addressed are the production and modification of interfaces and the creation of chemically and mechanically stable contact between active materials and solid electrolytes. Furthermore, the current state-of-the-art manufacturing techniques for SSB components (e.g., sol–gel, slurry coating by doctor blade deposition, spark plasma sintering, solution-based infiltration process, vapor deposition, screen-printing) come with higher costs, substantial capital investments, and reduced throughputs [10–15]. These are some of the key reasons why, globally, many end users are yet to realize the full potential of ASSBs in their products. Consequently, an alternative battery manufacturing technology, especially one that which can be readily industrialized, needs to be explored.

Plasma spray, one of the most widely utilized thermal spray techniques, can offer an alternative to overcome the above limitations, especially due to its huge potential to produce thin and multi-material coatings on a large scale with high throughput. So far, plasma spray has been explored for processing advanced ceramics for various applications such as solid-oxide fuel cells, thermal barrier coatings, solar cells, etc., with negligible efforts being made with regard to processing batteries. In particular, the recent emergent variant to plasma spraying which is "liquid feedstock plasma spraying" can provide immense possibilities towards processing some, if not all, of the ASSB constituents. Moreover, the recent development in the processing of multi-material coatings by simultaneously and/or sequentially injecting more than one material during the plasma spray process to produce multi-material, multilayer thin to thick coatings can also motivate industries and researchers to exploit this approach to manufacture complete ASSBs via plasma spraying [4,6–10].

However, due to the intrinsic nature of plasma-sprayed coatings, the presence of rough solid–solid interfaces, higher surface roughness, porosity, delamination, cracks, etc., leading to poor cohesion and adhesion is inevitable. In addition, extreme cooling rates involved during the rapid quenching of molten splats of ceramics during plasma spraying may change the crystallinity of the feedstock material. For instance, LTO has two different phase structures, rock-salt LTO ($Li_7Ti_5O_{12}$) and spinel LTO ($Li_4Ti_5O_{12}$), which are the desired phases of LTO for battery purposes [16]. These are some challenges that must be overcome to fully utilize this technology to produce ASSBs. Among existing routes, the laser processing of plasma-sprayed ASSB coatings can offer an exciting option to overcome the above challenges due to the possibility of localized thermal treatment to smoothen, densify, and recrystallize plasma-sprayed battery materials.

Laser processing, where a laser beam is selectively applied, is used not only to deposit or clad a thin or thick layer of ceramic, metallic, composite, etc., materials on different substrates, but also to build complex-shaped, additively manufactured components [17–19]. Furthermore, the laser beam provides thermal energy which can be used for processing, as utilized in this work to engineer the deposited surfaces. In general, laser processing has several variants such as laser heating, laser hardening, laser surface melting, laser forming, laser sintering, laser cleaning, etc. These variants have their own characteristics and effects which may lead to several advantages, including increasing the surface hardness and microstructure uniformity, strengthening metallurgical bonding to the substrate, better cohesion, minimal residual stresses, improved thermal fatigue resistance, wear behavior, recrystallization, etc. [20]. Specifically, laser processing can be used to reduce porosity in coatings, resulting in higher hardness, better corrosion resistance, decreased surface roughness, etc. [21]. All of these improved coating properties by laser post-processing can

play an important role in enhancing the performance of liquid feedstock plasma-sprayed ASSB constituents.

Therefore, in this work, as a novel post-processing technique aimed at altering the surface properties, we investigated the laser processing method to customize the surface characteristics of a suspension feedstock plasma-sprayed LTO SSB coating. Specifically, the effect of laser energy density or heat input on the characteristics of the suspension feedstock plasma-sprayed LTO battery coating was investigated. Among several variables, the two most important ones, laser power and laser processing speed, were studied, as well as their effect on coating characteristics such as microstructure, chemical composition, and roughness.

2. Materials and Methods

2.1. Materials

In the present study, lithium titanate ($Li_4Ti_5O_{12}$, LTO) powder with particle sizes ranging from 1.5 µm to 3.0 µm, obtained from NEI Corporation in the USA (Franklin Township, NJ, USA), was used as the anode material for deposition by plasma spraying. The substrate was commercially pure aluminum (Al) coupons which were 25 mm in diameter and 2 mm in thickness. Table 1 shows the chemical composition of the LTO powder as analyzed by energy-dispersive spectroscopy (EDS). Figure 1 depicts the morphology of the powder particles determined using a scanning electron microscope (SEM). The liquid feedstock was formulated in-house using the commercially available off-the-shelf powder mentioned below. The suspension was prepared in deionized water with 20 wt.% solid LTO powder and 1 wt.% 1-Methyl-2-pyrrolidinone (NMP) (Sigma-Aldrich, St. Louis, MO, USA) as an additive.

Table 1. Chemical composition of LTO powder and pure Al substrate measured by EDS.

Element	Li	Ti	O	Cl, Si, Al
LTO powder (wt.%)	not detectable	54.4	45.2	0.4

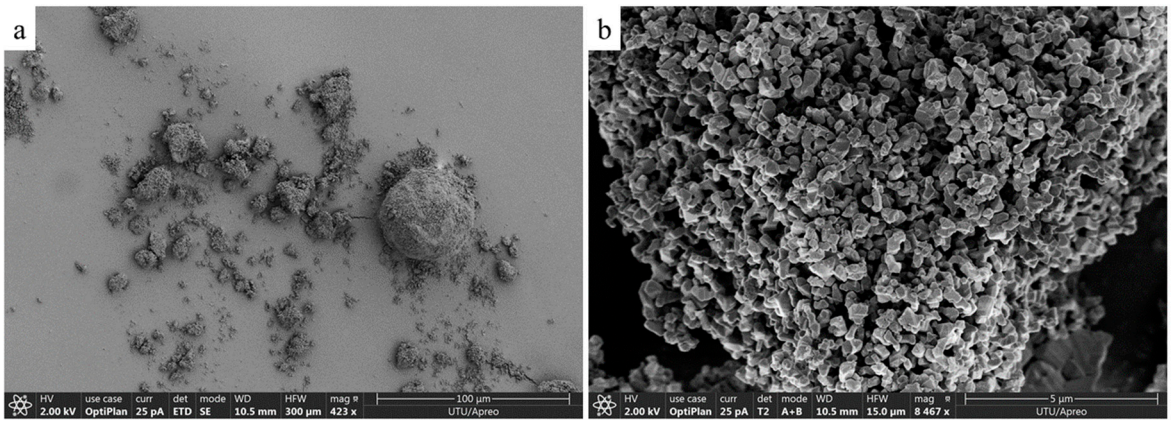

Figure 1. SEM micrographs at (**a**) low and (**b**) high magnifications revealing the irregular morphology of LTO powder particles.

2.2. Liquid Feedstock Plasma Spraying

The deposition of the LTO layer was obtained through liquid feedstock plasma spraying. The LTO layer was deposited using an Axial III high-power plasma torch, equipped with a Nanofeed 350 suspension feed system, provided by Northwest Mettech Corp, Surrey, BC, Canada. The plasma spray parameters utilized for the deposition of the LTO suspension are provided in Table 2. The spray passes were applied on top of each other.

Table 2. Plasma spray parameters utilized for deposition of LTO suspension.

Suspension Feed (mL/min)	Total Gas Flow (L/min)	Power (kW)	Enthalpy (kJ)	Number of Passes
42	200	110	11	20

2.3. Laser Processing

The energy input was the main variable varied in this study as calculated below. For instance, the energy (J) delivered to the material at a given location is as follows:

$$Energy(\mathrm{J}) = \frac{(P\ (\mathrm{W}))}{(Frequency\ (\mathrm{Hz}))} = P\ (\mathrm{W}) \times T\ (\mathrm{s}) \quad (1)$$

where T (s) is the interaction time spent by the laser beam to completely cross a precise point on the material, and its value can be approximated via the processing speed (PS) and laser beam diameter (D) using the following equation [22]:

$$T\ (\mathrm{s}) = \frac{D\ (\mathrm{m})}{PS\ (\mathrm{m/s})} \quad (2)$$

Assuming the circular projected laser beam of diameter D, the surface area is $A = \frac{\pi D^2}{4}$. Therefore, by combining Equations (1) and (2), the energy input becomes the following:

$$EI\ (\mathrm{J/m^2}) = \frac{4 \times Energy\ (\mathrm{J})}{\pi \times D^2} = \frac{4 \times Power\ (\mathrm{W})}{\pi \times D \times PS} \quad (3)$$

In the present work, the diameter of the laser beam (D) remained constant at 1 mm, while the laser power and processing speed were systematically varied to obtain different energy inputs. To create laser processing patterns on the surface of the plasma-sprayed sample, we employed multiple straight lines. Each of these lines was associated with a distinct energy density value. To maximize the treated areas on the sample and prevent any significant interaction between the scanned regions, we strategically spaced these lines far enough apart. To ensure that the laser achieved a steady-state condition before scanning a particular line, we initiated the laser exactly 4 mm prior to reaching the starting point of the designated line on the sample. The scanning direction proceeded from the outer edge of the sample towards the inner region.

A fiber laser with a maximum power of 10 kW (IPG photonics laser source, Marlborough, MA, USA) and an optical laser head were used for laser processing. More detailed experimental parameters of the fiber laser and optics are provided in Table 3.

Table 3. The specifications of laser equipment.

Laser YLS-10000-SM Class 4		PRECITEC Optical Head YW52	
Operating Wavelength (nm)	1070 ± 10	Focal length collimation (mm)	200
Mode of Operation	CW	Focal length focusing (mm)	400
Modulation Frequency (kHz)	0–5	Magnification multiplier	2
Power Tunability, %	10–100	Beam diameter (μm)	400
Power Stability, %	2	Rayleigh length (mm)	207.7
Laser Power [min–max] (kW)	0.08–10	Processing speed [min–max] (mm/s)	[0–50] (With robot)
Fiber Core Diameter, (μm)	200 (multi-mode)		

A total of 16 different lines were made on the plasma-sprayed coating; however, the present study focused on analyzing only four specific lines with substantial differences in energy densities, as shown in Table 4. The selection process of 4 lines was based on

not only visual aspects, but also on the evaluation of effects of the extremum comparable laser power and processing speed among 16 experimental conditions. A complete list of 16 varied parameter sets is provided in Table 4, and the selected lines focused on in the present study for characterization are highlighted in blue (i.e., lines a, f, h, and p). From here onwards, the selected lines a, f, h, and p are renamed as lines 1, 2, 3, and 4, respectively.

Table 4. Laser processing variables and laser-processed lines' positions and geometry on the plasma-sprayed sample. (Blue-highlighted rows are subjected for characterization).

Lines/Codes	Laser Power (W)	Process Speed (mm/s)	Energy Input (J/mm^2)
a (line 1)	200	0.25	1019.1
b	200	0.5	509.5
c	200	1	254.8
d	200	4	63.7
e	200	16	15.9
f (line 2)	200	50	5.1
g	80	0.125	815.5
h (line 3)	80	0.25	407.6
i	80	0.5	203.8
j	80	1	101.9
k	80	2	50.9
l	80	4	25.5
m	80	8	12.7
n	80	16	6.4
o	80	32	3.2
p (line 4)	80	50	2.1

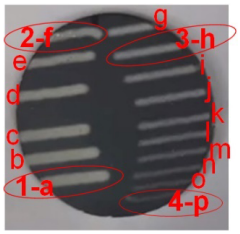

2.4. Characterization

Scanning electron microscopy (SEM) was performed using an APREO field emission SEM (FE-SEM) (Thermo Fisher Scientific, Waltham, MA, USA) equipped with an EDS detector. SEM analysis was carried out using a lower acceleration voltage of 5 kV, whereas for EDS analysis, it was set to 15 kV or 20 kV. The ImageJ software (ver. 1.53q) was used to determine the width of laser-processed lines. This involved measuring 5 distinct sections of each line to evaluate the average widths of each. Additionally, the Alicona Infinite Focus G6 (Bruker, Billerica, MA, USA) optical 3D measurement system based on laser imaging with MetMax software (ver. 3.0) was used to assess the surface topography and roughness of laser-processed lines and non-laser-processed areas. The Sa values of roughness measurements were evaluated. The roughness average (Sa) is a dispersion parameter defined as the mean of the absolute values of the surface departure above and below the mean plane within the sampling area [23].

3. Results and Discussion

3.1. Laser-Processed Zone Morphology and Geometry

Four laser track lines were examined through SEM analysis, as depicted in Figure 2. The results revealed noticeable morphological differences between the region in the laser post-processing zone and the non-laser-processed zone (which corresponded to the as-sprayed area). However, an evident enhancement in surface smoothness was observed within the laser-processed area, leading to surfaces that appeared comparatively smoother compared to the as-sprayed regions.

The effect of energy input on the interaction width of the laser beam and plasma-sprayed LTO surface was also studied. As shown in Figure 3, it is obvious that an increase in energy density led to an increase in the average width of laser-processed zones. However, careful observation suggested that the real effect of power on line width was significantly

higher as compared to the process speed. For instance, comparing line 1 and line 4, the change in line width was about 2.5-fold, corresponding to a 200-fold change in speed and a 500-fold change in energy density. However, in this situation, the change in power was only two and a half times.

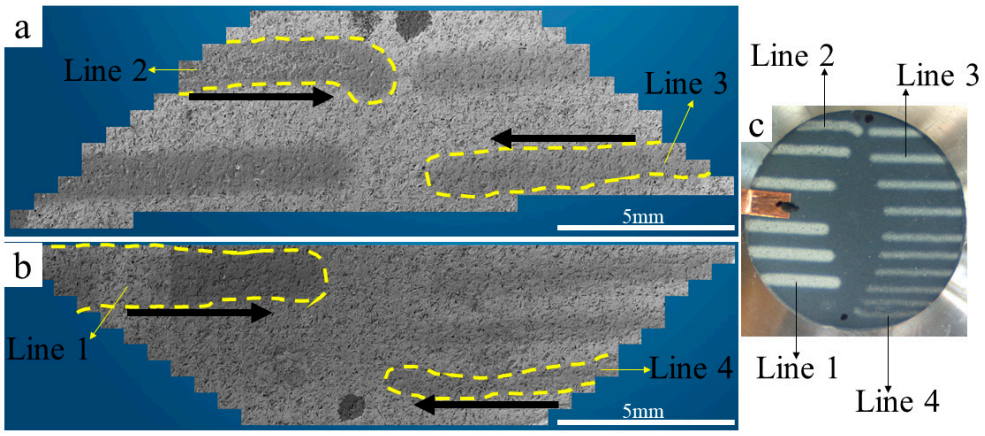

Figure 2. Stitched top-surface SEM images of (**a**) upper and (**b**) lower half of the laser-processed sample, (**c**) navigation SEM image of whole sample, where the black arrows shown the laser processing direction.

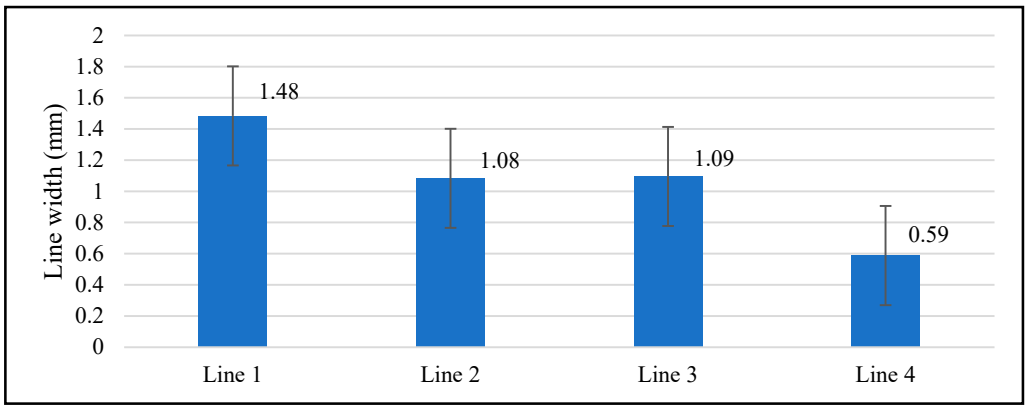

Figure 3. The average width of laser-processed lines.

The presence of a rough surface in as-sprayed regions was evident from the surface topography images obtained from a three-dimensional optical profilometer, which are shown in Figure 4. This behavior is typically seen in plasma-sprayed ceramic coatings [24]. The presence of hilly areas (as can be seen in Figure 2) is even more prominent in liquid feedstock plasma-sprayed ceramic coatings, which is due to the formation of so-called cauliflower or columnar structures. The formation of these cauliflower or columnar structures is due to the low-momentum atomized liquid droplet trajectories following the plasma stream and subsequent shadowing effect with the asperities of substrate resulting in the formation of such hilly regions [25,26]. In Figure 5, the color gradations ranging from orange to yellowish and green–green–blue–magenta represent the variation in surface topography, transitioning from hilly to valley regions. The blue color indicates the base plane of the surface. The presence of distinct spikes, referred as hilly areas (green color), was evident in the as-sprayed sample, evident from the maximum roughness height of 238.274 µm (please see Figure 6), contributing to surface roughness of 7.84 µm. In contrast, during laser processing, the interaction of the laser with the hills caused the melting of hills and subsequent filling of valleys. This change was observable through patches of yellowish-green color contour, indicating the formation of a melt pool during laser processing. Furthermore, the depth of scanning was reduced to 96.891 µm (please see Figure 6) for

laser-processed as-sprayed coatings. Laser processing had a noticeable impact on reducing the surface roughness of as-sprayed coatings. For instance, in line 2, the lowest surface roughness was observed at 5.87 µm, as evidenced by large yellowish-green patches with a scanning depth of 96.891 µm (please see Figure 6).

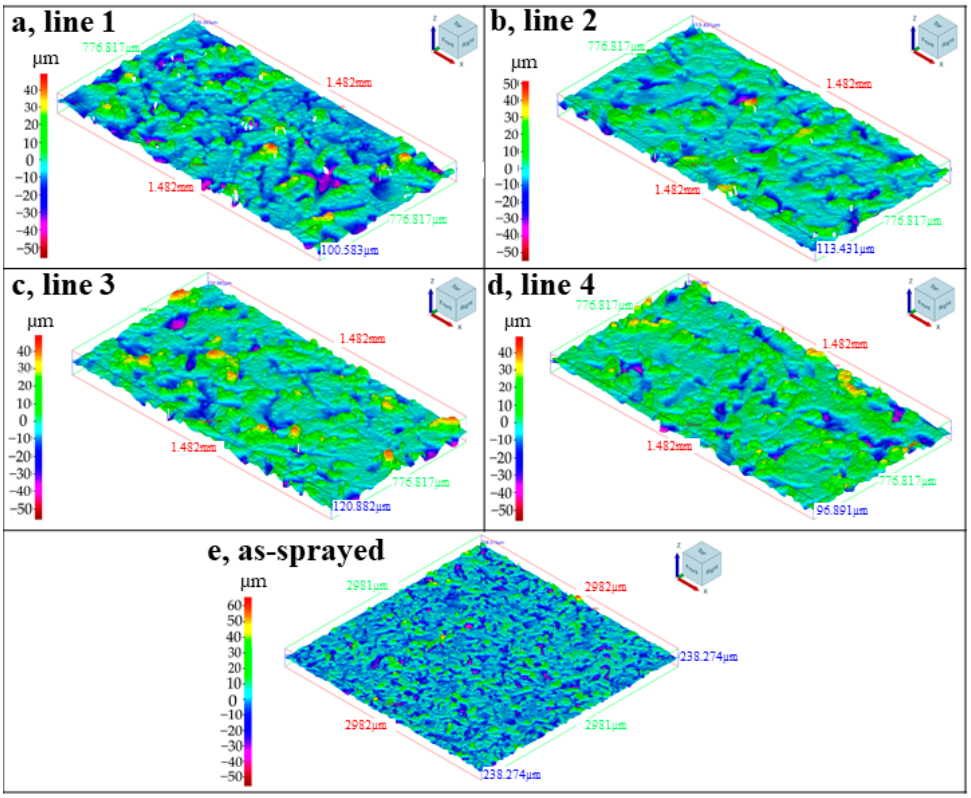

Figure 4. Surface topography imaged using optical profilometry from central area of laser-processed lines on plasma-sprayed sample: (**a**) line 1, (**b**) line 2, (**c**) line 3, (**d**) line 4, and (**e**) as-sprayed area (non-laser-processed).

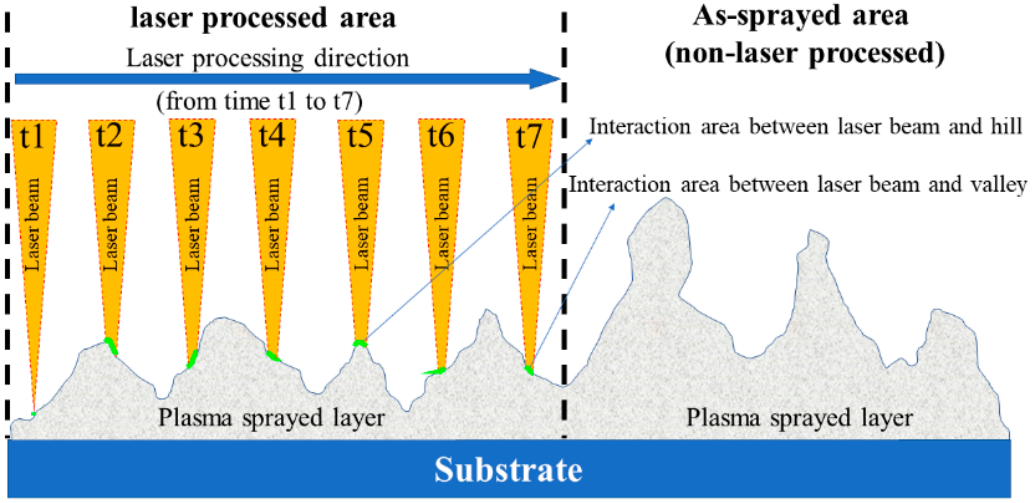

Figure 5. Illustration depicting interaction of laser beam with hill and valley areas on the plasma-sprayed surface.

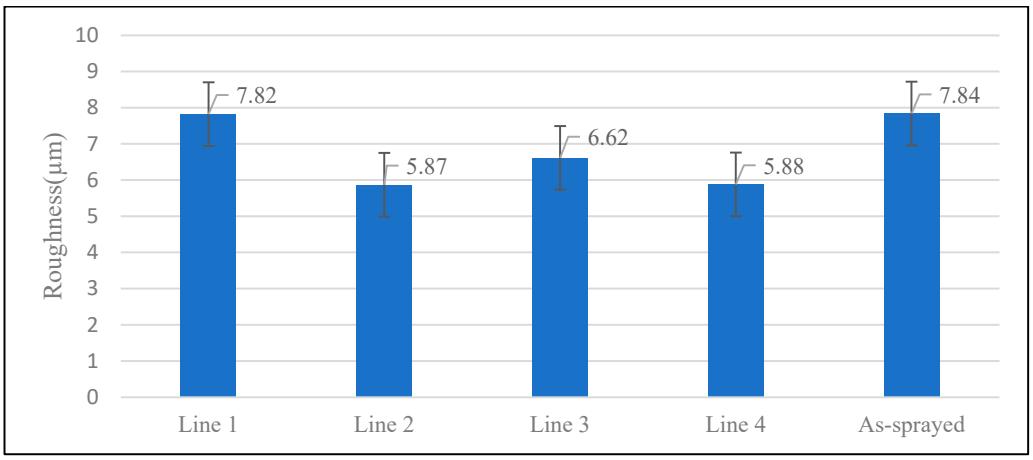

Figure 6. Sa roughness values for the laser-processed and as-sprayed regions.

According to the illustration provided in the schematic (Figure 5), as the laser beam traveled in a straight line across the plasma-sprayed region which consisted of alternating hills and valleys, there was a possibility that the beam primarily interacted with the elevated hills rather than the valleys. This possibility was greater when the laser spot with lower energy moved faster across the surface, providing insufficient time for the heat to dissipate across the surface and interact with the entire area, thereby limiting modifications to the surface morphologies.

The variations in roughness measurements observed in laser-processed coatings are closely tied to variations in the laser-processing parameters. As is evident in Figures 4 and 6, laser processing led to lower roughness (Sa) values across all lines compared to the as-sprayed (non-laser post-processed) area, particularly for line 1, which had very high energy input. This indicates that laser post-processing has an effective role in smoothing the surface of plasma-sprayed SSB coatings. Furthermore, when comparing line 2 and line 4, both of which were subjected to the same energy input range, the Sa values were almost the same. Nonetheless, line 2 had a scanning depth of 113.431 µm, while line 4 had a scanning depth of 96.891 µm, highlighting the clear differences in surface topography. This distinction was also evident in the optical profilometry images, as illustrated in Figure 4b for line 2 and Figure 4d for line 4. In the case of line 3 and line 1, both of which shared the same laser speed (0.25 mm/s), line 1 utilized a higher laser power (200 W) compared to line 3 (80 W). Consequently, line 1 exhibited higher roughness (7.82 µm) compared to line 3 (6.62 µm). Notably, line 2 showed the lowest roughness, while line 1 demonstrated the highest roughness. This corresponds to the outcomes of the study, as both line 1 and line 3, treated with higher laser energy density (1019.1 J/mm^2 and 407.6 J/mm^2, respectively) and a slower laser processing speed (0.25 mm/s), exhibited notably higher surface roughness of 7.823 µm and 6.62 µm, respectively, compared to line 2 (5.87 µm) and line 4 (5.88 µm).

Thus, these findings strongly support the hypothesis proposed in this study, indicating that when a laser beam with lower power interacts at a faster rate on a rough surface, there is a limited time for heat to absorb and dissipate and influence the entire scanned region. Consequently, significant alterations to the surface are restricted. It should be mentioned that for a fixed laser power, the scanning speed should be optimum, so that the interaction time of the laser beam with the peak of hills is suitable enough and the hills can be partially melted to fill the valleys (see Figure 5). However, decreasing the scanning speed to below the optimum value can cause increased spatters and turbulence in melted zones due to excessive energy input, and consequently, the surface roughness will be increased [27], as seen in line 1.

The surface of the LTO plasma-sprayed sample subjected to laser processing was further analyzed using SEM, as shown in Figure 7 with the example of line 2. As discussed earlier, an improvement in surface smoothness is observed through the laser processed

line, and this enhanced smoothness became even more evident when inspecting higher-magnification SEM micrographs, as shown in Figure 7, where a highlighted area marked by yellow dotted lines clearly demonstrates this effect. Furthermore, the surface topography appeared to be a non-uniform, rough surface both before and after processing. However, as indicted in Figure 7c, the presence of lake-shape melted zones within the laser-processed lines led to some degree of surface smoothening. The plasma-sprayed coating surface showed regions with non-uniform surfaces with hills, valleys, pores, etc. Nonetheless, laser processing effectively eliminated pores, hills, and valleys, resulting in the emergence of localized smoothed regions. Additionally, mud cracks were also observed in such smoothened areas, as shown in Figure 7e. Mud cracks are commonly found in ceramics [28]. Nevertheless, such cracks can also be observed in laser-processed areas. This is attributed to the thermal stress caused by the large temperature gradient between the ceramic coating and metallic substrate during laser treatment, as well as the non-uniform dissipation of incident laser energy from the plasma-sprayed ceramic coating in both the longitudinal and transverse directions [26]. When considering the laser heat treatment process, particularly in single-track investigations or mesoscale examinations of ceramics within laser-based additive manufacturing (AM) processes, transverse cracks typically initiate from the sides of the sample and propagate along the direction of the laser scan. It is worth noting that these cracks do not follow a straight path but often exhibit local deflections. During the propagation of these cracks, there is a tendency for bifurcation to occur, leading to the formation of secondary cracks, and in some cases, even tertiary cracks, as shown in Figure 7e. Conversely, in macro-scale studies, particularly when layers are stacked atop each other (layer by layer) in ceramics, as is commonly seen in laser AM processes, longitudinal cracks become more prominent. Ceramics are inherently more susceptible to developing cracks. The ideal scenario involves preheating the substrate/sample followed by laser heat treatment [29]. In Figure 7f,g, pits are shown, which are frequently encountered in laser-based processes [30–33]. The formation of such particular morphology in this region can be attributed to the melting and solidification during laser processing. The extremely high surface temperature in the melting zone resulted in the gasification of some materials, leading to the formation of such large pores. In other words, due to the porous microstructure of plasma-sprayed LTO, the formation of pits can be related to the fact that gas bubbles cannot completely escape from the melt pool during laser processing. Marangoni force, temperature gradients in the atmosphere, melt pool, substrate, and low-density bubbles are the driving forces behind bubble movements inside a melt pool.

Discernible defects in the form of pinholes and microcracks were expected on the uneven surface of the as-sprayed coatings, as highlighted in a relevant reference. This specific structure is a common characteristic of plasma-sprayed coatings, primarily due to the inherent nature of the plasma-spray process, resulting in a lamellar microstructure intertwined with micro-defects, as is evident in our plasma-sprayed LTO coating.

Conversely, after laser heat treatment, the expectation was a noticeable reduction in pores and voids formed during the plasma spray process. However, variations in laser parameters, such as power and scanning speed, influenced the interaction of the laser beam with the plasma-sprayed region, particularly in the alternating hills and valleys. There was a possibility that the laser beam primarily interacted with the elevated hills rather than the valleys, especially when the laser spot with lower energy moved faster across the surface, providing insufficient time for heat dissipation and interaction with the entire area. This limitation may account for the observed minimal modifications to the surface.

These types of investigations aim to eliminate differences between the laser-processed and non-laser-processed zones and provide a more comprehensive understanding of the impact of laser parameters on surface modifications [34]. During the last stage of the solidification process, these bubbles also tend to release from the melt pool at the melt pool–atmosphere interface [33]. Lower scanning speeds or higher laser power contributed to the reduced viscosity and surface tension of the molten LTO. Consequently, the localized melting or decomposition of the LTO ultimately resulted in a discontinuous melt pool.

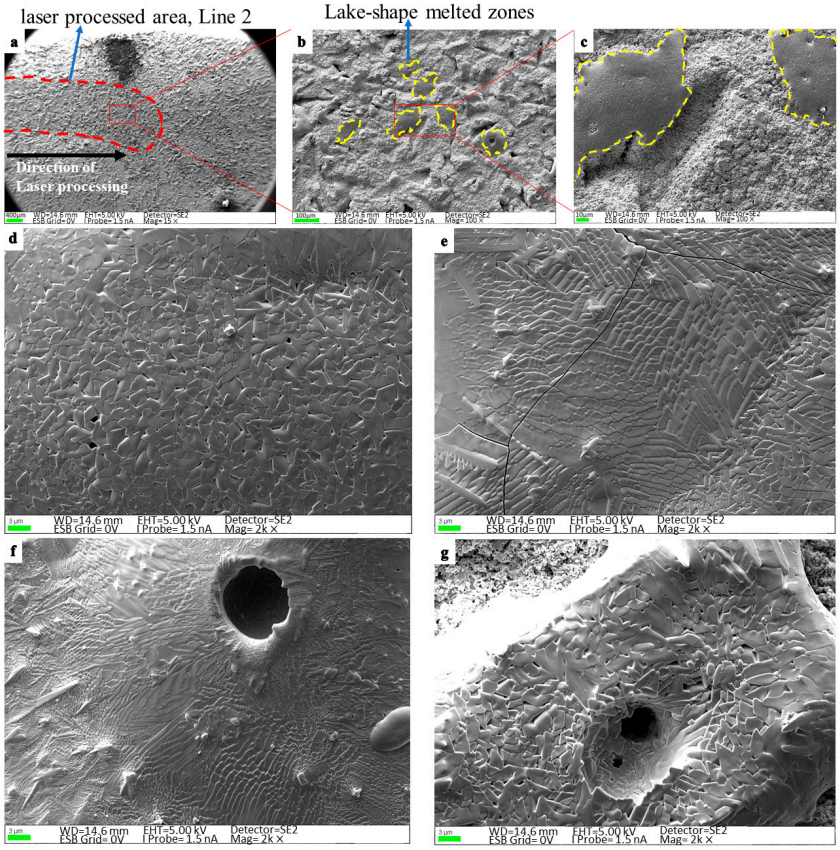

Figure 7. The surface topography of line 2 plasma-sprayed laser-processed zone, (**a**) 16× mag., (**b**) 100× mag., (**c**) 500× mag., (**d**) 2k× mag., (**e**) presence of cracks, (**f**,**g**) pits.

Regarding the grain structure in the laser-processed regions, the SEM micrograph revealed a compelling insight into the intricate details. The morphology displayed was notably flat and dense, aligning precisely with the direction of heat flow experienced during laser processing. Notably, within the lake-shaped melted laser-processed regions, a distinctive grain type emerged, characterized by an equiaxed structure.

The genesis of such a unique grain formation can be attributed to the variance in solidification rates within the laser-processed area. Ceramic materials like LTO exhibit a proclivity towards columnar dendritic solidification when confronted with a low cooling or solidification rate. Conversely, under high solidification rates, a tendency towards an equiaxed microstructure becomes apparent.

As illustrated in Figure 7d,e, the rapid cooling mechanism manifests in the observation of an equiaxed flake-shaped or faceted microstructure [35]. This nuanced understanding of the grain evolution in laser-processed areas sheds light on the material's response to differing solidification rates, offering valuable insights for further analysis and optimization.

3.2. Elemental Distribution

The chemical composition of the as-sprayed, laser-processed, and non-laser-processed zones is depicted in Figure 8 and summarized in Table 5. It is evident that there were no substantial differences among them.

It is indeed apparent that laser heat treatment had an impact on the elemental distribution of the samples. However, it is crucial to emphasize that our primary objective was to preserve the spinel phase composition (LTO) for applications in charging/discharging (energy storage).

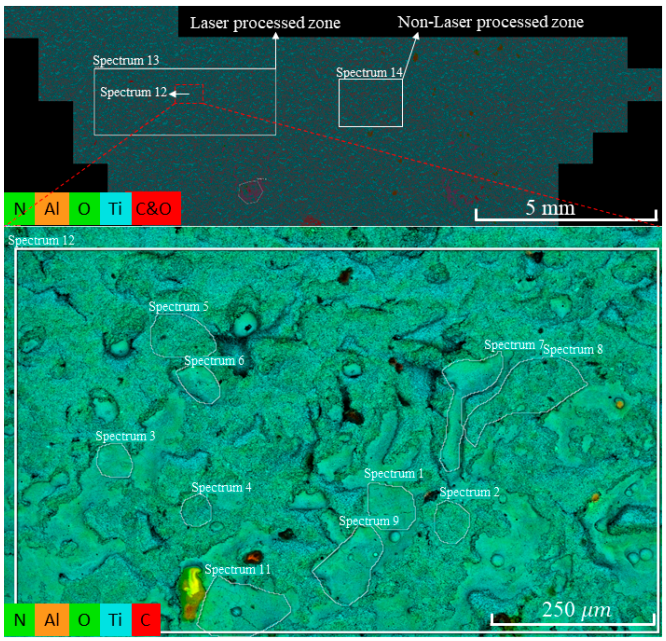

Figure 8. Elemental mapping of laser-processed and non-laser-processed zones in line 1. To discern the composition of the distinct regions, multiple localized spectra were also recorded within the analyzed region of Spectrum 12.

Table 5. Elemental composition comparison different zones in line 1 (Li could not be detected).

			Ti (wt.%)	O (wt.%)	C (wt.%)
Non-laser-processed (As-sprayed area)	Spectrum 14		59.5	35.6	3.3
Laser-processed area	Spectrum 12		55	37.8	6.5
	Lake-shape melted zones	Spectrum 1	51	39.5	9.5
		Spectrum 3	52	38.2	9.8
		Spectrum 6	55.2	35.1	9.7
		Spectrum 7	56.1	36.5	7.4
		Spectrum 9	55.3	35.6	8.5
		Spectrum 11	53.3	37.6	8.7
		Average composition	53.8	37.1	8.9
	Non-melted zones	Spectrum 2	54.6	41.8	3.6
		Spectrum 4	54.8	39.2	6
		Spectrum 5	54	39.8	6.2
		Spectrum 8	55.3	38.8	6
		Average composition	54.7	39.9	5.4

Note: Li element could not be detected since it is beyond the detection limit of EDS.

The laser parameters employed in our study clearly indicate that we have achieved this goal, as evidenced by the presence of titanium and oxygen, leading to the presence of the spinel phase (though further investigation is warranted). It is worth mentioning that the current characterization technique has limitations in detecting lithium content.

On average, the titanium (Ti) content in the laser-processed areas was slightly lower than in as-sprayed areas, and this was vice versa for carbon (C) content. Also, due to laser irradiation during laser processing in unprotected ambient conditions, oxidation occurred,

and the oxygen (O) content was increased in the laser-processed areas. To limit oxidation, this process should be carried out in inert or vacuum atmospheres.

Furthermore, in the laser-processed areas, some lake-shape melted zones had higher C content and lower Ti content. This was because of more complex and higher concentrations of alloying elements which led to lower melting points, so the regions with higher C content melted more easily and sooner than the other regions.

It is important to highlight that ongoing research is focused on comprehending the impact of laser processing on the elemental constitution of LTO (lithium titanate) material. For example, any modifications that facilitate the formation of Ti^{3+} sites in lithium titanate would enhance its physical and electrochemical properties. In this context, C doping has shown promise in reducing particle size and particle agglomeration. Consequently, non-metallic doping has proven to be highly effective in enhancing both the capacity and rate performance of lithium titanate [36].

4. Conclusions

In the present study, a comparative investigation has been conducted to assess the effect of laser processing on liquid feedstock plasma-sprayed Lithium Titanium Oxide (LTO) as a potential material for solid-state-battery electrodes. Specifically, the effect of changes in laser power and processing speed on the geometry, morphology, and elemental distribution on the coating surface were investigated. The following conclusions are drawn from the results of the present investigations:

1. Laser processing resulted in the surface smoothening of the LTO plasma-sprayed coating layer. Additionally, the use of laser power led to the formation of lake-shaped melted regions, contributing to surface smoothing.
2. The effect of changes in laser power on the width of laser-processed lines and the percentage of melted zones was significantly higher than the effect of changes in laser processing speed.
3. While the differences in the chemical composition of the coating before and after laser processing were not significant, there was a noticeable increase in oxygen content in the laser-processed regions of the LTO coating. This can be attributed to laser irradiation and the substantial heat input.
4. A localized higher concentration of light elements such as oxygen was noted in the lake-shaped melted zones after laser processing.

These conclusions emphasize the potential applications of laser-processed LTO coatings in the development of improved solid-state-battery electrodes.

Author Contributions: Conceptualization: A.H., A.S., S.G., and A.G.; formal analysis: A.H., M.L., and A.G.; funding acquisition: S.G. and A.G.; investigation: A.H., M.L., and N.K.; methodology: A.H., M.L., N.K., and A.G.; project administration: A.G.; resources: A.H., S.J., and A.G.; supervision: S.J., S.G., and A.G.; validation: A.H.; writing—original draft: A.H., M.L., N.K., and C.N.; writing—review and editing: A.H., N.K., C.N., S.J., A.S., S.G., and A.G. All authors have read and agreed to the published version of the manuscript.

Funding: This research was funded by the project GREEN-BAT [26081094, 2022–2025], under the framework of M-ERA.Net. Authors would like to Thank Academy of Finland and M-ERA.NET 3 from the European Commission and the respective national/regional financier. The Swedish segment of this research conducted at University West, Sweden has been made possible by funding received from the following projects: (a) a proof-of-concept project NovelCABs supported by Energimyndigheten, the Swedish Energy Agency, Dnr 2021-002227 and (b) a trans-national M-ERA.NET 3 project Green-BAT with support from the European Commission and the respective national/regional financiers with Vinnova (Swedish Governmental Agency for Innovation Systems) being the national financier for Swedish participation.

Institutional Review Board Statement: Not applicable.

Informed Consent Statement: Not applicable.

Data Availability Statement: The authors confirm that the data supporting the findings of this study are available within the article.

Acknowledgments: The authors would like to acknowledge the support of Aki Piiroinen for his valuable assistance in the laser processing step and Ermei Mäkilä for his great assistance during the SEM/EDS characterization step. The authors would also like to thank Stefan Björklund from University West, Trollhättan, Sweden, for plasma spraying the battery materials.

Conflicts of Interest: The authors declare no conflicts of interest.

References

1. Tarascon, J.-M.; Armand, M. Issues and challenges facing rechargeable lithium batteries. *Nature* **2001**, *414*, 359–367. [CrossRef]
2. Pacala, S.; Socolow, R. Stabilization Wedges: Solving the Climate Problem for the Next 50 Years with Current Technologies. *Science* **2004**, *305*, 968–972. [CrossRef]
3. Nitta, N.; Wu, F.; Lee, J.T.; Yushin, G. Li-ion battery materials: Present and future. *Mater. Today* **2015**, *18*, 252–264. [CrossRef]
4. Kammampata, S.P.; Garakani, M.A.; Zhang, Z.; Thangadurai, V. Solid-state electrolytes for lithium-ion batteries. In *Comprehensive Inorganic Chemistry III*; Elsevier: Amsterdam, The Netherlands, 2023; pp. 658–680. [CrossRef]
5. Kurzweil, P.; Garche, J. Overview of batteries for future automobiles. In *Lead-Acid Batteries for Future Automobiles*; Elsevier: Amsterdam, The Netherlands, 2017; pp. 27–96. [CrossRef]
6. Wang, L.; Li, J.; Lu, G.; Li, W.; Tao, Q.; Shi, C.; Jin, H.; Chen, G.; Wang, S. Fundamentals of Electrolytes for Solid-State Batteries: Challenges and Perspectives. *Front. Mater.* **2020**, *7*, 111. [CrossRef]
7. Boaretto, N.; Garbayo, I.; Valiyaveettil-SobhanRaj, S.; Quintela, A.; Li, C.; Casas-Cabanas, M.; Aguesse, F. Lithium solid-state batteries: State-of-the-art and challenges for materials, interfaces and processing. *J. Power Sources* **2021**, *502*, 229919. [CrossRef]
8. Pasta, M.; Armstrong, D.; Brown, Z.L.; Bu, J.; Castell, M.R.; Chen, P.; Cocks, A.; Corr, S.A.; Cussen, E.J.; Darnbrough, E.; et al. 2020 roadmap on solid-state batteries. *J. Phys. Energy* **2020**, *2*, 032008. [CrossRef]
9. Yang, Y. A mini-review: Emerging all-solid-state energy storage electrode materials for flexible devices. *Nanoscale* **2020**, *12*, 3560–3573. [CrossRef] [PubMed]
10. McOwen, D.W.; Xu, S.; Gong, Y.; Wen, Y.; Godbey, G.L.; Gritton, J.E.; Hamann, T.R.; Dai, J.; Hitz, G.T.; Hu, L.; et al. 3D-Printing Electrolytes for Solid-State Batteries. *Adv. Mater.* **2018**, *30*, e1707132. [CrossRef] [PubMed]
11. Famprikis, T.; Canepa, P.; Dawson, J.A.; Islam, M.S.; Masquelier, C. Fundamentals of inorganic solid-state electrolytes for batteries. *Nat. Mater.* **2019**, *18*, 1278–1291. [CrossRef] [PubMed]
12. Yamamoto, M.; Takahashi, M.; Terauchi, Y.; Kobayashi, Y.; Ikeda, S.; Sakuda, A. Fabrication of composite positive electrode sheet with high active material content and effect of fabrication pressure for all-solid-state battery. *J. Ceram. Soc. Jpn.* **2017**, *125*, 391–395. [CrossRef]
13. Gao, Z.; Sun, H.; Fu, L.; Ye, F.; Zhang, Y.; Luo, W.; Huang, Y. Promises, Challenges, and Recent Progress of Inorganic Solid-State Electrolytes for All-Solid-State Lithium Batteries. *Adv. Mater.* **2018**, *30*, e1705702. [CrossRef]
14. Zaman, W.; Hatzell, K.B. Processing and manufacturing of next generation lithium-based all solid-state batteries. *Curr. Opin. Solid State Mater. Sci.* **2022**, *26*, 101003. [CrossRef]
15. Lobe, S.; Bauer, A.; Uhlenbruck, S.; Fattakhova-Rohlfing, D. Physical Vapor Deposition in Solid-State Battery Development: From Materials to Devices. *Adv. Sci.* **2021**, *8*, 2002044. [CrossRef] [PubMed]
16. Sorensen, E.M.; Barry, S.J.; Jung, H.-K.; Rondinelli, J.M.; Vaughey, J.T.; Poeppelmeier, K.R. Three-Dimensionally Ordered Macroporous $Li_4Ti_5O_{12}$: Effect of Wall Structure on Electrochemical Properties. *Chem. Mater.* **2005**, *18*, 482–489. [CrossRef]
17. Moradi, M.; Hasani, A.; Pourmand, Z.; Lawrence, J. Direct laser metal deposition additive manufacturing of Inconel 718 superalloy: Statistical modelling and optimization by design of experiments. *Opt. Laser Technol.* **2021**, *144*, 107380. [CrossRef]
18. Moradi, M.; Hasani, A.; Beiranvand, Z.M.; Ashoori, A. Additive manufacturing of stellite 6 superalloy by direct laser metal deposition—Part 2: Effects of scanning pattern and laser power reduction in different layers. *Opt. Laser Technol.* **2020**, *131*, 106455. [CrossRef]
19. Moradi, M.; Pourmand, Z.; Hasani, A.; Moghadam, M.K.; Sakhaei, A.H.; Shafiee, M.; Lawrence, J. Direct laser metal deposition (DLMD) additive manufacturing (AM) of Inconel 718 superalloy: Elemental, microstructural and physical properties evaluation. *Optik* **2022**, *259*, 169018. [CrossRef]
20. Han, Q.; Jiao, Y. Effect of heat treatment and laser surface remelting on AlSi10Mg alloy fabricated by selective laser melting. *Int. J. Adv. Manuf. Technol.* **2019**, *102*, 3315–3324. [CrossRef]
21. Stutzman, A.; Rai, A.; Alexandreanu, B.; Albert, P.; Sun, E.; Schwartz, M.; Reutzel, E.; Tressler, J.; Medill, T.; Wolfe, D. Laser glazing of cold sprayed coatings for the mitigation of stress corrosion cracking in light water reactor (LWR) applications. *Surf. Coat. Technol.* **2020**, *386*, 125429. [CrossRef]
22. Suder, W.J.; Williams, S.W. Investigation of the effects of basic laser material interaction parameters in laser welding. *J. Laser Appl.* **2012**, *24*, 032009. [CrossRef]
23. Semnani, D. Geometrical characterization of electrospun nanofibers. In *Electrospun Nanofibers*; Elsevier: Amsterdam, The Netherlands, 2017; pp. 151–180. [CrossRef]
24. Ganvir, A. *Design of Suspension Plasma Sprayed Thermal Barrier Coatings*; University West: Trollhättan, Sweden, 2018.

25. Ganvir, A.; Calinas, R.F.; Markocsan, N.; Curry, N.; Joshi, S. Experimental visualization of microstructure evolution during suspension plasma spraying of thermal barrier coatings. *J. Eur. Ceram. Soc.* **2019**, *39*, 470–481. [CrossRef]
26. Zhang, X.; Chen, L. Effects of laser scanning speed on surface roughness and mechanical properties of aluminum/Polylactic Acid (Al/PLA) composites parts fabricated by fused deposition modeling. *Polym. Test.* **2020**, *91*, 106785. [CrossRef]
27. Chen, T.; Gong, B.; Tang, C. Origin and Evolution of Cracks in the Glaze Surface of a Ceramic during the Cooling Process. *Materials* **2023**, *16*, 5508. [CrossRef]
28. Su, H.; Liu, H.; Jiang, H.; Shen, Z.; Chen, Q.; Yu, M.; Zhao, D.; Li, X.; Dong, D.; Zhang, Z. One-step preparation of melt-grown $Al_2O_3/GdAlO_3/ZrO_2$ eutectic ceramics with large size and irregular shape by directed energy deposition. *Addit. Manuf.* **2023**, *70*, 103563. [CrossRef]
29. Liu, H.; Su, H.; Shen, Z.; Zhao, D.; Liu, Y.; Guo, M.; Guo, Y.; Zhang, J.; Liu, L.; Fu, H. Effect of scanning speed on the solidification process of $Al_2O_3/GdAlO_3/ZrO_2$ eutectic ceramics in a single track by selective laser melting. *Ceram. Int.* **2019**, *45*, 17252–17257. [CrossRef]
30. Liu, H.; Su, H.; Shen, Z.; Wang, E.; Zhao, D.; Guo, M.; Zhang, J.; Liu, L.; Fu, H. Direct formation of $Al_2O_3/GdAlO_3/ZrO_2$ ternary eutectic ceramics by selective laser melting: Microstructure evolutions. *J. Eur. Ceram. Soc.* **2018**, *38*, 5144–5152. [CrossRef]
31. Gu, D.; Hagedorn, Y.-C.; Meiners, W.; Meng, G.; Batista, R.J.S.; Wissenbach, K.; Poprawe, R. Densification behavior, microstructure evolution, and wear performance of selective laser melting processed commercially pure titanium. *Acta Mater.* **2012**, *60*, 3849–3860. [CrossRef]
32. Triantafyllidis, D.; Li, L.; Stott, F. Mechanisms of porosity formation along the solid/liquid interface during laser melting of ceramics. *Appl. Surf. Sci.* **2003**, *208–209*, 458–462. [CrossRef]
33. Zhou, L.; Yuan, T.; Li, R.; Tang, J.; Wang, G.; Guo, K. Selective laser melting of pure tantalum: Densification, microstructure and mechanical behaviors. *Mater. Sci. Eng. A* **2017**, *707*, 443–451. [CrossRef]
34. Arshad, A.; Yajid, M.A.M.; Daroonparvar, M.; Idris, M.H.; Zulkifli, I.S.M.; Hassan, A.G.; Halim, Z.A.A. Effect of Laser-Glazed Treatment on Thermal Cyclic Behavior of Plasma-Sprayed Lanthanum Zirconate/Yttria-Stabilized Zirconia Double Ceramic Layered on NiCoCrAlYTa-coated Inconel. *J. Therm. Spray Technol.* **2023**, *32*, 2603–2619. [CrossRef]
35. Liu, G.; Li, J.; Chen, K.; Chen, Y.; Jiang, Z.; Song, Y. Microstructure evolution of ceramic materials during solidification from melts in high-gravity combustion synthesis. *Mater. Res. Bull.* **2012**, *47*, 222–234. [CrossRef]
36. Li, Y.; Gao, H.; Yang, W. Enhancements of the structures and electrochemical performances of Li4Ti5O12 electrodes by doping with non-metallic elements. *Electrochim. Acta* **2022**, *409*, 139993. [CrossRef]